

Electro-reduction of carbon dioxide at low over-potential at a metal-organic framework decorated cathode

Xinchen Kang ¹, Lili Li¹, Alena Sheveleva ¹, Xue Han¹, Jiangnan Li¹, Lifei Liu², Floriana Tuna ^{1,3}, Eric J. L. McInnes ¹, Buxing Han²✉, Sihai Yang ¹✉ & Martin Schröder ¹✉

Electrochemical reduction of carbon dioxide is a clean and highly attractive strategy for the production of organic products. However, this is hindered severely by the high negative potential required to activate carbon dioxide. Here, we report the preparation of a copper-electrode onto which the porous metal-organic framework [Cu₂(L)] [H₄L = 4,4',4'',4'''-(1,4-phenylenebis(pyridine-4,2,6-triyl))tetrabenzoic acid] can be deposited by electro-synthesis templated by an ionic liquid. This decorated electrode shows a remarkable onset potential for reduction of carbon dioxide to formic acid at -1.45 V vs. Ag/Ag⁺, representing a low value for electro-reduction of carbon dioxide in an organic electrolyte. A current density of 65.8 mA·cm⁻² at -1.8 V vs. Ag/Ag⁺ is observed with a Faradaic efficiency to formic acid of 90.5%. Electron paramagnetic resonance spectroscopy confirms that the templated electro-synthesis affords structural defects in the metal-organic framework film comprising uncoupled Cu(II) centres homogeneously distributed throughout. These active sites promote catalytic performance as confirmed by computational modelling.

¹Department of Chemistry, University of Manchester, Manchester M13 9PL, UK. ²Beijing National Laboratory for Molecular Sciences, CAS Key Laboratory of Colloid, Interface and Chemical Thermodynamics, Institute of Chemistry, Chinese Academy of Science, 100190 Beijing, China. ³Photon Science Institute, University of Manchester, Manchester M13 9PL, UK. ✉email: hanbx@iccas.ac.cn; Sihai.Yang@manchester.ac.uk; M.Schroder@manchester.ac.uk

Increasing CO₂ levels in the atmosphere present significant environmental impacts^{1–3}. Thus, routes to carbon capture and storage, as well as development of CO₂ reduction technologies to afford chemical feedstocks are being developed^{4–6}. Reduction of CO₂ is economically and environmentally desirable but technically challenging because the high energy of the C=O bond (750 kJ·mol⁻¹) makes it an extremely stable molecule that is reluctant to transform^{7–9}. One effective method to overcome the high activation barrier is through electrochemical catalytic reduction in which CO₂ is reduced under mild conditions^{10–13}. Copper-based electrodes have been reported as powerful catalysts for the electro-reduction of CO₂ to give numerous products including CO, formic acid and, recently, C₂ and other products^{14–18}. Formic acid is heavily used in chemical industries for leather, dyeing and textiles, and can be converted directly within fuel cells^{13,19}, and is therefore a valuable C₁ product. Reduction of CO₂ at Cu-based electrodes can proceed via O-bound HCOO⁻ or C-bound -COOH intermediates that are formed from electrochemically generated ·CO₂⁻ radicals. The latter route can diverge to other possible products^{20,21}, but the electro-reduction of CO₂ via an O-bound HCOO⁻ pathway may enhance the Faradaic efficiency for the formation of formic acid. In addition, the formation of formic acid requires a highly negative potential for CO₂ reduction, and this often leads to decomposition of copper-based catalyst via reduction of metal sites during electrolysis. Although emerging electrocatalysts have been reported for reduction of CO₂ to formic acid at low over-potentials¹⁷, more work needs to be undertaken to understand the details of this catalysis^{22,23}.

In recent years, there has been much interest in metal-organic framework (MOF) materials as crystalline porous hosts for gas adsorption, separation and catalysis^{24–26}. Their high surface area, potentially active metal centres, diverse pore structure and, in exceptional cases, their redox activity, promote their use as electrocatalysts for H₂ and O₂ evolution and reduction of O₂^{27–29}. However, highly crystalline MOFs with fully coordinated metal centres exhibit only low charge-transfer ability and formally no active centres for electrocatalysis¹². Therefore, in order to drive efficient electrocatalysis, MOFs that exhibit high capacity for charge-transfer and incorporate accessible metal sites are highly desirable.

Herein, we report the templated electrochemical growth of the Cu(II) complex [Cu₂(L)] [H₄L = 4,4',4'',4'''-(1,4-phenylenebis(pyridine-4,2,6-triyl))tetrabenzoic acid] (Supplementary Fig. 1) on a Cu-foam electrode to introduce abundant structural defects comprised of active Cu(II) sites within the deposited film. The resultant electrode, Cu₂(L)-e/Cu, shows excellent activity for the reduction of CO₂ to formic acid with an onset potential of -1.45 V vs. Ag/Ag⁺ for production of formic acid, a Faradaic efficiency (FE_{HCOOH}) reaching 90.5% at -1.8 V vs. Ag/Ag⁺ and a current density of 65.8 mA·cm⁻². Side reactions, such as H₂ evolution and reduction of Cu(II) sites, are effectively hindered at low potentials, and the catalytic mechanism has been studied by electron paramagnetic resonance (EPR) spectroscopy and density functional theory (DFT) calculations.

Results and discussion

Electrosynthesis of Cu₂(L)-e/Cu. The ligand H₄L was synthesised via a three-step method from our previous report³⁰. The electrode, Cu₂(L)-e/Cu, was prepared by electro-synthesis of the MOF on Cu-foam at a potential of 8.0 V at 60 °C in the presence of the ionic liquid 1-ethyl-3-methylimidazolium acetate (EmimOAc, Supplementary Fig. 2) as supporting electrolyte (Supplementary Fig. 3). Upon completion, the porous Cu-foam was uniformly coated with green crystallites of Cu₂(L)-e (Fig. 1a–d) thus limiting the further supply of Cu²⁺ ions from the anode for

synthesis of more MOF material. SEM images confirm the spherical morphology of the complex film with an average particle size of ~50 nm (Fig. 1e, f). For comparison, the MOF was also synthesised by a conventional solvothermal reaction [denoted as Cu₂(L)-t]³¹, which crystallised in much larger octahedral-shaped crystals of several microns in size (Supplementary Fig. 4). The structure of Cu₂(L) comprises of a 3D network built around binuclear [Cu₂(OOCR)₄] paddlewheels with four bridging carboxylate ligands (Fig. 1g, h)³².

Structural analysis and characterisation of Cu₂(L). Power X-ray diffraction (PXRD) confirmed that Cu₂(L)-t and Cu₂(L)-e (removed from the electrode) have the same structure consistent with the simulated pattern (Fig. 2a)³¹. We sought to characterise the nature of the structural defects in Cu₂(L)-e, which can be captured vividly by confocal fluorescence microscopy (CFM) using the oligomerisation of furfuryl alcohol as a probe³³. In this case, open Cu(II)-site based defects act as Lewis acid centres that catalyse the formation of oligomers of furfuryl alcohol to generate strong fluorescence. The microphotographs and CFM images show (Fig. 2b, c) fluorescence evenly across particles of Cu₂(L)-e, whereas only the surfaces of Cu₂(L)-t exhibit fluorescence, confirming the wide distribution of open Cu(II) defect sites throughout Cu₂(L)-e. Fourier transform infrared (FTIR) spectroscopy shows that the ν(C=O) stretching vibration of the carboxylate group in Cu₂(L)-e is blue shifted by 17 cm⁻¹, from 1385 cm⁻¹ to 1402 cm⁻¹, compared to Cu₂(L)-t, consistent with increased amounts of unbound carboxylate groups in the former (Fig. 2d). A slight decrease in decomposition temperature for Cu₂(L)-e compared to Cu₂(L)-t by TGA analysis suggests that the defect structure of Cu₂(L)-e has slightly reduced thermal stability (Fig. 2e). Full elemental analysis of these materials reveals a Cu:L ratio of 2.4 in Cu₂(L)-e (Supplementary Table 1), higher than the 2.0 ratio obtained for Cu₂(L)-t. This reflects the direct growth of Cu₂(L)-e onto the Cu-foam surface to give a more Cu-rich environment. X-band and Q-band EPR spectra at room temperature reveal a significantly greater concentration of uncoupled Cu(II) defect sites in Cu₂(L)-e than in Cu₂(L)-t (Fig. 2f, g, Supplementary Figs. 5–8). The spectra are dominated by the characteristic spin triplet spectrum of the [Cu₂(OOCR)₄] paddlewheel structure, which arise from strong antiferromagnetic exchange (singlet-triplet gap *ca.* 300 cm⁻¹) within the binuclear moiety and the thermal population of the excited S = 1 state, which has a zero-field splitting of *ca.* 0.3 cm⁻¹. The characteristic forbidden transition (*m_S* = ±2) associated with the triplet spin state of the Cu₂ entity is clearly observed (*ca.* 5300 G) in all Q-band spectra of Cu₂(L)-e and Cu₂(L)-t (Fig. 2g and Supplementary Fig. 8). In addition, features due to uncoupled Cu(II) (*S* = ½, *g_{xx,yy}* = 2.07, *g_{zz}* = 2.32, *A_{xx,yy}*^{Cu} = 33.6 MHz, and *A_{zz}*^{Cu} = 450 MHz) ions are observed (*ca.* 3250 G at X-band; 12000 G at Q-band), and these signals are more pronounced in Cu₂(L)-e than in Cu₂(L)-t (Fig. 2f, g). The relative concentration of [Cu₂(OOCR)₄] paddlewheel units and uncoupled free Cu(II) is given by the relative intensity of the second integral of simulations of the Q-band EPR spectra, weighted by the room temperature Boltzmann population of the spin triplet state of the [Cu₂(OOCR)₄] paddlewheel (Fig. 2h, i and Supplementary Table 2)^{34–36}. Using this approach it was determined that Cu₂(L)-t and Cu₂(L)-e contain 1.5% and 15.3% of uncoupled Cu(II) sites, respectively, confirming that electro-synthesis generates an order of magnitude greater number of defect sites.

Analysis of porosity in Cu₂(L). The porosity of these MOFs was studied by N₂ isotherms at 77 K (Fig. 2j and Supplementary Table 1). Desolvated Cu₂(L)-t shows a Type-I sorption profile

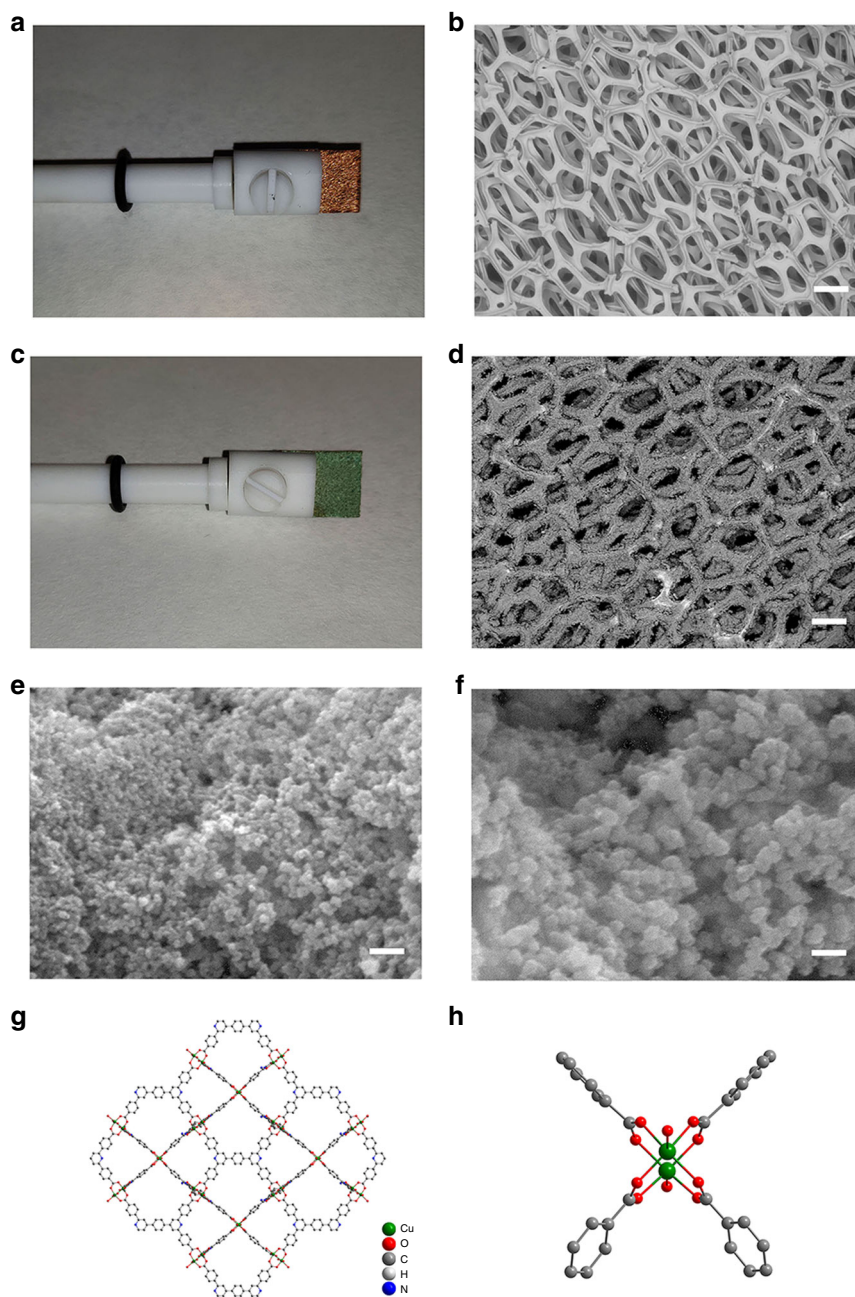


Fig. 1 Images and morphology. **a, b** Photograph (**a**) and SEM image (**b**) of a fresh Cu-foam electrode ($0.5 \times 1.0 \text{ cm}^2$). **c** Photograph of the as-prepared electrode $\text{Cu}_2(\text{L})\text{-e}/\text{Cu}$ ($0.5 \times 1.0 \text{ cm}^2$). **d-f** SEM images of the as-prepared electrode $\text{Cu}_2(\text{L})\text{-e}/\text{Cu}$. **g-h** Views of the crystal structure of $[\text{Cu}_2(\text{L})]$ (CCDC 1531622)³¹. Hydrogen atoms are omitted for clarity. The scale bars of **b, d-f** are $300 \mu\text{m}$, $300 \mu\text{m}$, 300 nm and 100 nm , respectively.

consistent with the expected uniform microporosity. In contrast, desolvated $\text{Cu}_2(\text{L})\text{-e}$ exhibits a profile between Type-I and Type-IV, suggesting the presence of both mesopores and micropores. The distribution of micro- and mesopores within both materials has been analysed by Horvath-Kawazoe and Barrett–Joyner–Halenda (BJH) methods, respectively (Fig. 2k, l). The reduction in micropores in $\text{Cu}_2(\text{L})\text{-e}$ results in a low N_2 uptake at low pressure, while $\text{Cu}_2(\text{L})\text{-e}$, generated by the template-effect of the ionic liquid during electro-synthesis³³, shows a total pore volume of $1.89 \text{ cm}^3 \cdot \text{g}^{-1}$, significantly larger than that of $\text{Cu}_2(\text{L})\text{-t}$ ($0.32 \text{ cm}^3 \cdot \text{g}^{-1}$), reflecting the presence of mesopores in $\text{Cu}_2(\text{L})\text{-e}$. CO_2 adsorption in desolvated $\text{Cu}_2(\text{L})\text{-t}$ and $\text{Cu}_2(\text{L})\text{-e}$ at 1.0 bar and 298 K are 38.5 and $44.7 \text{ cm}^3 \cdot \text{g}^{-1}$, respectively (Fig. 2m). Higher isosteric heats of adsorption (Q_{st})

were obtained for $\text{Cu}_2(\text{L})\text{-e}$ (Supplementary Figs. 9, 10), suggesting stronger interactions with CO_2 than in $\text{Cu}_2(\text{L})\text{-t}$, consistent with the presence of additional active sites in the former. In summary, electro-synthesised $\text{Cu}_2(\text{L})\text{-e}$ can be grown directly onto Cu-foam to afford a decorated electrode incorporating a defect structure with active Cu(II) sites that show strong interaction with CO_2 , a key feature for an optimal catalyst for CO_2 reduction³⁷. For comparison, the benchmark system HKUST-1 has also been electro-synthesised onto Cu-foam (denoted as HKUST-1-e/Cu) using the same method, and fully characterised by SEM, PXRD, TGA and BET (Supplementary Figs. 11–14 and Supplementary Table 1). High crystallinity and large particle sizes ($\sim 1 \mu\text{m}$) were obtained for HKUST-1-e, consistent with its facile crystal growth.

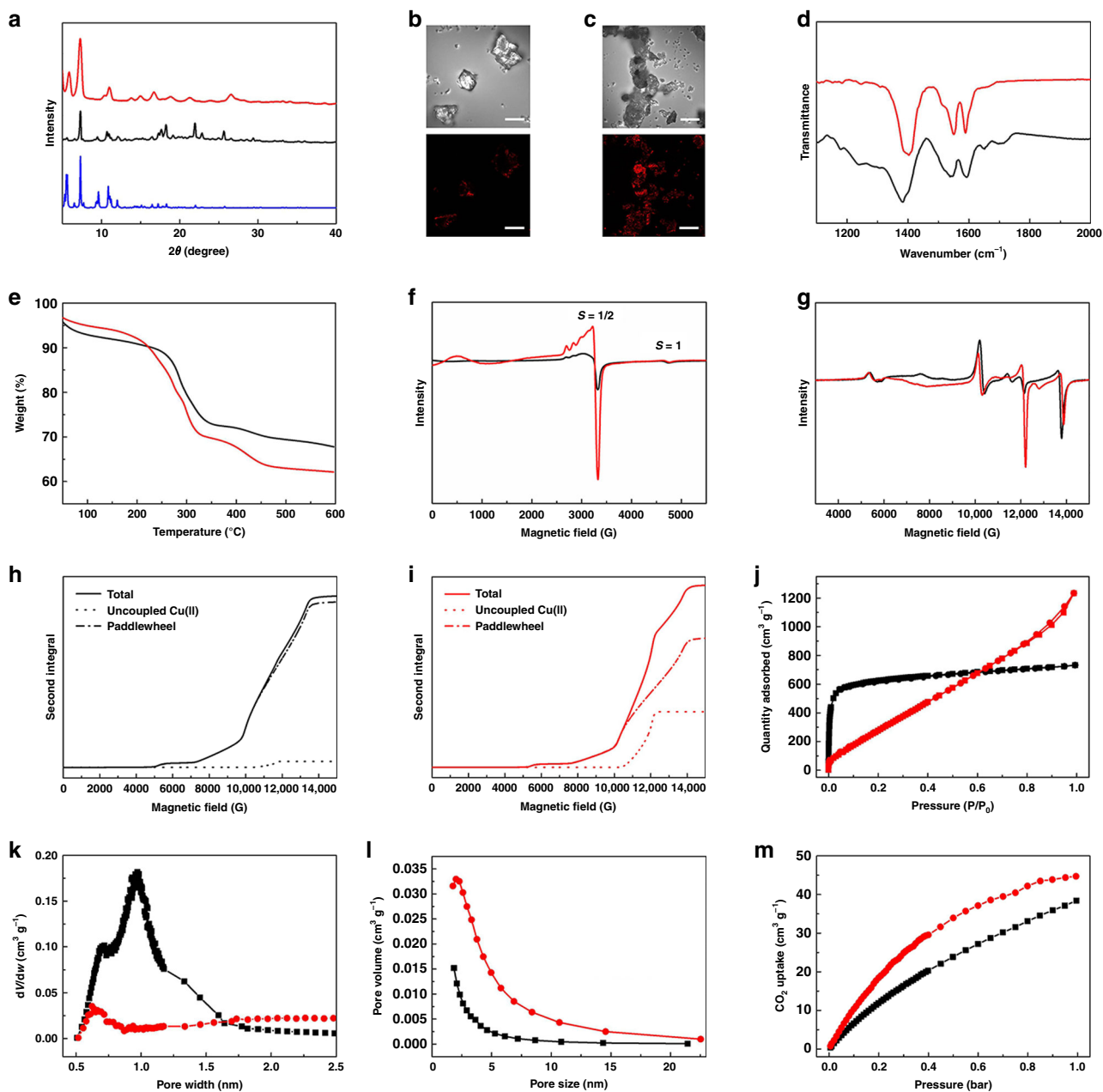


Fig. 2 Characterisations of $\text{Cu}_2(\text{L})\text{-t}$ (black lines) and $\text{Cu}_2(\text{L})\text{-e}$ (red lines). **a** PXRD patterns (blue line refers to simulated PXRD pattern). The defects in $\text{Cu}_2(\text{L})\text{-e}$ result in broadening of peaks due to poorer crystallinity of the material. **b** Micrograph (top) and CFM image (bottom) of $\text{Cu}_2(\text{L})\text{-t}$. The fluorescence (shown in red colour) indicates the presence of crystal defects determined by the oligomerisation of furfuryl alcohol. **c** Micrograph (top) and CFM image (bottom) of $\text{Cu}_2(\text{L})\text{-e}$. **d** Selected FTIR spectra (full spectra are shown in Supplementary Information). **e** TGA curves. **f** X-band EPR spectra at room temperature. **g** Q-band EPR spectra at room temperature. **h** Second integrals from simulated Q-band EPR spectra for $\text{Cu}_2(\text{L})\text{-t}$. **i** Second integrals from simulated Q-band EPR spectra for $\text{Cu}_2(\text{L})\text{-e}$. **j** N_2 adsorption/desorption isotherms at 77 K. **k** Micropore size distribution. **l** Mesopore size distribution. **m** Adsorption isotherms for CO_2 at 298 K (desorption data are shown in Supplementary Information). Data for HKUST-1-e are shown in Supplementary Information. The scale bars of **b** and **c** are 20 μm .

Electrochemical reduction of CO_2 . To test performance for electrochemical reduction of CO_2 , $\text{Cu}_2(\text{L})\text{-e}/\text{Cu}$ and HKUST-1-e/ Cu were used directly as electrodes, while a powder sample of $\text{Cu}_2(\text{L})\text{-t}$ was loaded onto carbon paper (CP) with Nafion-D521 as adhesive to fabricate a $\text{Cu}_2(\text{L})\text{-t}/\text{CP}$ electrode¹². All experiments were performed in an H-type cell with 0.5 M 1-ethyl-3-methylimidazolium tetrafluoroborate (EmimBF_4) in acetonitrile (0.5 M $\text{EmimBF}_4/\text{MeCN}$) as catholyte. As shown from the linear sweep voltammetry at the $\text{Cu}_2(\text{L})\text{-e}/\text{Cu}$ electrode, negligible current was generated in N_2 -saturated electrolyte, while the current

density increased dramatically in CO_2 -saturated electrolyte, confirming a strong response to CO_2 (Supplementary Fig. 15). The dependence of current density on time ($i\text{-t}$ curves) for all three electrodes is shown in Fig. 3a. Minimal current density was observed with N_2 , whereas a rise in current density is observed on introduction of CO_2 . The current density continuously increases in the presence of CO_2 and stabilises after 1 h for the three electrodes. The $\text{Cu}_2(\text{L})\text{-e}/\text{Cu}$ electrode shows the highest current density, and for all systems, formic acid was found to be the only carbon-containing product based on GC and ^1H NMR

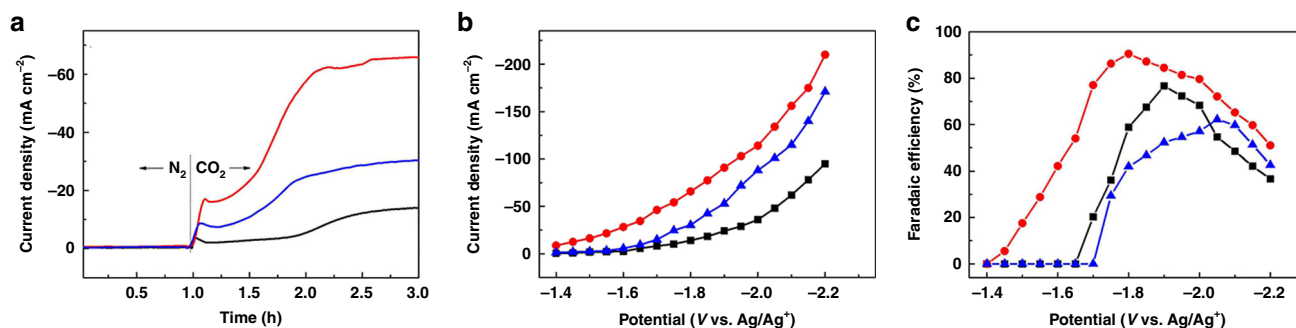


Fig. 3 Electrochemical reduction of CO₂ over Cu₂(L)-t/CP (black lines), Cu₂(L)-e/Cu (red lines), and HKUST-1-e/Cu (blue lines). **a** Plot of current density vs. time. **b** Plot of current density vs. potential. **c** Plot of FE_{HCOOH} vs. potential.

spectroscopic analysis of gas and liquid phases, respectively, after electrolysis. No carbon-containing product was detected in the absence of CO₂ from the catholyte, confirming that the generated formic acid is derived solely from introduced CO₂ rather than decomposition of the catalyst or electrolyte. The current density and Faradaic efficiency for formation of formic acid (FE_{HCOOH}) were recorded after 2 h of electrolysis (Fig. 3b, c) from -1.4 V to -2.2 V vs. Ag/Ag⁺. H₂ is the only bi-product within this potential range. Significantly, the Cu₂(L)-e/Cu electrode shows an onset potential of -1.45 V vs. Ag/Ag⁺ for the generation of formic acid, representing one of the lowest potential observed in organic electrolytes for systems reported to date (Supplementary Table 3)^{6,38–40}, although a recent Cu-porphyrin system shows an onset voltage as low as -1.4 V vs. Ag/Ag⁺.¹⁷ The current density increases with increasing negative potential, but FE_{HCOOH} increases and then decreases, reaching a maximum of 90.5% at -1.8 V vs. Ag/Ag⁺ with a current density of 65.8 mA·cm⁻². The value of FE_{HCOOH} is maintained at >80% between -1.75 V to -1.95 V vs. Ag/Ag⁺. In comparison, the Cu₂(L)-t/CP electrode exhibits a higher onset potential of -1.7 V vs. Ag/Ag⁺ for formic acid production and a lower current density across the potential range, with a maximum FE_{HCOOH} of 77% observed at -1.9 V vs. Ag/Ag⁺. For the HKUST-1-e/Cu electrode, an even higher onset potential of -1.75 V vs. Ag/Ag⁺ was observed for production of formic acid, and FE_{HCOOH} reaches a maximum of 62% at -2.05 V vs. Ag/Ag⁺. Thus, Cu₂(L)-e/Cu demonstrates an excellent performance for electro-reduction of CO₂ in terms of the low onset potential and high FE_{HCOOH} with relatively low over-potentials. The current density for formic acid production increases rapidly from the onset potential to -2.0 V vs. Ag/Ag⁺, and the production of formic acid progresses slowly thereafter (Supplementary Fig. 16), reflecting the enhanced production of H₂ at potentials more negative than -2.0 V vs. Ag/Ag⁺. At potentials more negative than -2.0 V vs. Ag/Ag⁺, the HKUST-1-e/Cu electrode shows a rise in current density (Fig. 3b) with the current density of formic acid reaching a plateau (Supplementary Fig. 16). An undecorated Cu-foam electrode (Fig. 1a, b) was also tested, and a current density of 4.2 mA·cm⁻² with a FE_{HCOOH} of 20.5% after 2 h electrolysis at -1.8 V vs. Ag/Ag⁺ were observed (Supplementary Fig. 17), demonstrating the critical role of defect Cu₂(L) on the performance of the electrode. It should be noted that a nanostructured Cu-foam has been explored previously as an electrocatalyst¹⁶; the Cu-foam in the current study is of a different type and is much smoother.

Upon completion of reaction, HKUST-1-e turned amorphous and partially peeled off the Cu-foam as confirmed by SEM images. In contrast, Cu₂(L)-e/Cu generally maintained its morphology with a slight aggregation of particles (Supplementary Fig. 18). Thus, the thin coating with small crystallites in the Cu₂(L)-e/Cu electrode affords chemical and mechanical stability

for electrolysis, although like many Cu(II) MOFs¹⁵, the Cu₂(L)-e/Cu electrode is unstable in water.

Variations of EPR spectra of electrodes over time. To understand further the mechanism of catalysis of these electrodes, EPR spectra were measured over time intervals of 15 mins during electrolysis of CO₂ at -1.8 V vs. Ag/Ag⁺. We sought to use EPR spectroscopy to probe changes in concentrations of free, uncoupled Cu(II) centres as the reaction proceeds⁴¹, and this can be monitored by the relative intensity of the second integral of the EPR spectrum (Fig. 4a). As confirmed above, as-prepared Cu₂(L)-e/Cu has a high concentration of uncoupled Cu(II) centres due to its defect structure. All three electrodes show an increase in uncoupled Cu(II) content during electrolysis: this is presumably caused by reduction of the [Cu₂(OOCR)₄] paddlewheel units under the electrolytic conditions, with subsequent structural disruption. The amount of free Cu(II) sites was maximised after electrolysis for 75, 60 and 45 mins for Cu₂(L)-e/Cu, Cu₂(L)-t/CP and HKUST-1-e/Cu, respectively, followed by a slight decrease for Cu₂(L)-e/Cu and a greater decrease in Cu₂(L)-t/CP and HKUST-1-e/Cu. The quantities of uncoupled Cu(II) sites decrease after a maximum and are likely due to reduction to diamagnetic (3d¹⁰) Cu(I) over time (Supplementary Fig. 19), as confirmed by XPS and Auger spectra (Supplementary Fig. 20). These results also support the thesis that free Cu(II) defect sites are responsible for the high current density and FE_{HCOOH} observed for Cu₂(L)-e/Cu throughout the electrolysis of CO₂ (Fig. 4b, c). H₂ evolution becomes more evident over time using Cu₂(L)-t/CP and HKUST-1-e/Cu electrodes also likely due to generation of Cu(I) sites over time (Supplementary Fig. 21). The reduction of [Cu₂(OOCR)₄] paddlewheel MOFs to form Cu(II). Cu(I) species has been reported previously⁴², and is associated with tetrahedral distortion of the reduced metal centre to give an uncoupled Cu(II) centre. The current density for formation of formic acid remains constant after the uncoupled Cu(II) content reaches its maximum value, and so catalysis remains stable up to 5 h (Supplementary Figs. 22, 23). Thus, Cu₂(L)-e/Cu exhibits the best performance for long-term electrochemical stability for formic acid production. It is notable that the total Faradaic efficiency for formation of formic acid and H₂ (FE_{HCOOH+H2}) is lower than 100% during the first hour of electrolysis (Supplementary Fig. 24), indicating that the electrode evolves during this early period of electrolysis, consistent with the morphological changes observed at the electrode surface (Supplementary Fig. 18).

Electrochemical characteristics of electrodes. The charge-transfer ability of the electrode also plays an important role in its electrocatalytic performance. As revealed by Nyquist plots at an open circuit potential (Fig. 4d), the Cu₂(L)-e/Cu, Cu₂(L)-t/CP

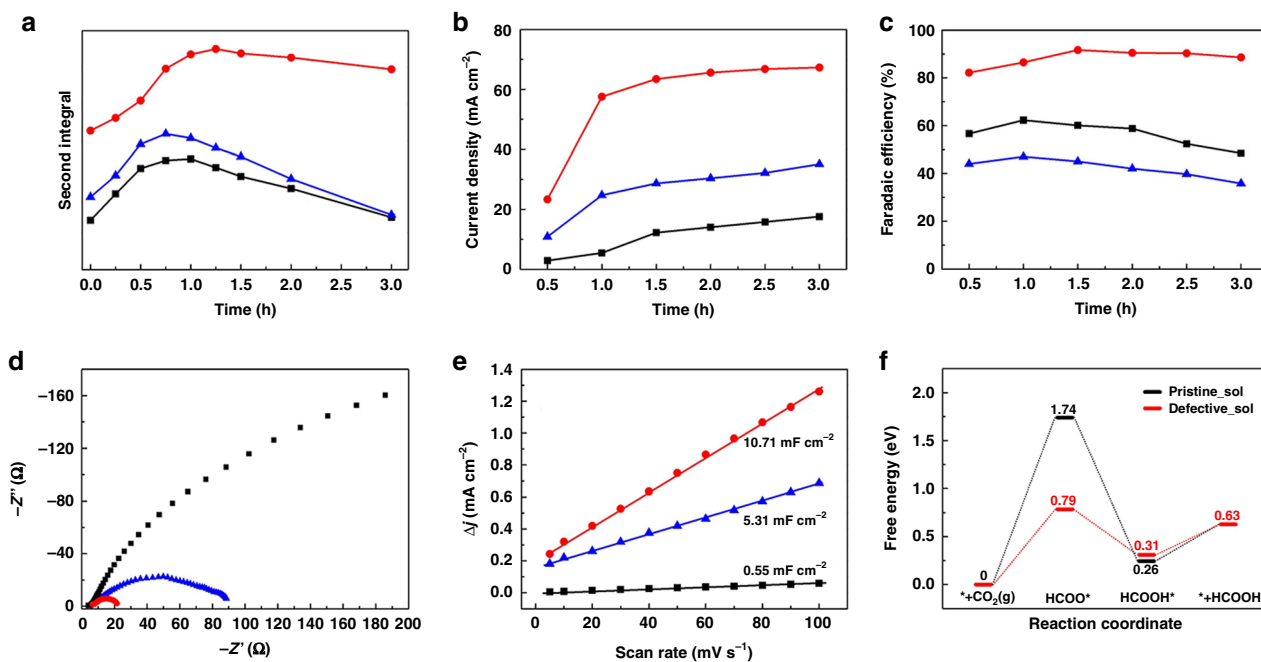


Fig. 4 Comparisons of Cu₂(L)-t/CP (black lines), Cu₂(L)-e/Cu (red lines) and HKUST-1-e/Cu (blue lines). **a**, Plot of second integral of the X-band EPR signals for uncoupled Cu(II) centres at room temperature vs. time of CO₂ electrolysis. **b** Plot of current density vs. time of CO₂ electrolysis at -1.8 V vs. Ag/Ag⁺. **c** Plot of FE_{HCOOH} vs. time of CO₂ electrolysis at -1.8 V vs. Ag/Ag⁺. **d** Nyquist plots for reduction of CO₂. **e** Plot of difference in charging current density vs. scan rates. **f** DFT calculation of Gibbs free energy of electro-reduction of CO₂ to formic acid over pristine (black lines) and defect Cu₂(L)-t (red lines) after consideration of solvation effects.

and HKUST-1-e/Cu electrodes give charge-transfer resistances (R_{ct}) of approximately 17, 114 and 408 Ω, respectively^{12,38}. The significantly lower R_{ct} for Cu₂(L)-e/Cu is most likely due to its microscopic morphology as revealed from SEM images. Thus, nanoparticles of Cu₂(L) form a compact thin coating on the Cu-foam surface with the overall porous network preserved, whereas rapid crystallisation of HKUST-1 results in bigger crystals and a thick coating of HKUST-1-e/Cu, leading to a higher overall resistance. The poorly-conductive MOF islands on the HKUST-1-e/Cu electrodes thus cause barriers for charge-transfer, in sharp contrast to Cu₂(L)-e/Cu, where all MOF particles are in close contact with the highly conductive Cu-foam. The interface between Cu₂(L)-t and CP results in the poor charge-transfer as observed in many other MOF-based electrodes¹². The double-layer capacitance (C_{dl}) of the three electrodes was analysed by measuring the capacitive current associated with double-layer charging using the scan-rate dependence of cyclic voltammetric stripping to evaluate the electrochemical active surface area (Fig. 4e)⁴³. Cu₂(L)-e/Cu has the highest value for C_{dl} of 10.71 mF·cm⁻² with values for Cu₂(L)-t/CP and HKUST-1-e/Cu of 5.31 mF·cm⁻² and 0.55 mF·cm⁻², respectively, again evidencing the high active surface area of Cu₂(L)-e/Cu^{44,45}.

DFT calculations. DFT calculations have been applied widely to uncover the mechanism of electro-reduction of CO₂^{46–48}. The Gibbs free energy with respect to potential reaction steps was modelled based upon a [Cu₂(OOCR)₄] paddlewheel bound to four 4-(pyridin-2-yl)benzoate groups. Pristine and defect structures representing Cu₂(L)-t and Cu₂(L)-e, respectively, were then analysed by DFT calculations with defect Cu₂(L) modelled with one of the O-donors of one 4-(pyridin-2-yl)benzoate not bound to Cu(II) to afford a vacant site at Cu(II). The corrections for zero point energy and entropy, and the structural model and atomic coordinates of all intermediates are given in Supplementary Tables 4–12. The plausible reaction pathways via C-bound

COOH and O-bound HCOO intermediates were analysed (Supplementary Figs. 25, 26) and the effects of solvation were also taken into account (Supplementary Fig. 27). In general, the formation of O-bound HCOO involved a lower Gibbs free energy than C-bound COOH or CO over both pristine and defect Cu₂(L), with formation of O-bound HCOO on defect Cu₂(L) the most facile pathway leading to selective production of formic acid. In the DFT calculations the free Cu(II) centres in defect Cu₂(L) are generated by the rupture of one Cu–O(carboxylate) bond, which enables binding of CO₂ via an O-bound HCOO intermediates. In addition, the defect structure leads to weaker hydrogen bonding between the MOF and product, facilitating the release of HCOOH from the surface of the Cu₂(L)-e/Cu electrode. The same pattern of Gibbs free energy is also observed on inclusion of solvation effects (Supplementary Fig. 27). Figure 4f shows the DFT calculated diagram of Gibbs free energy of electro-reduction of CO₂ to formic acid over pristine and defect Cu₂(L) with solvation effects considered. Furthermore, both Cu₂(L)-t and Cu₂(L)-e electrodes show an increase in uncoupled Cu(II) content during electrolysis (Fig. 4a), consistent with the increasing current density for CO₂ reduction observed over the first hour of electrolysis. Hydrogen evolution was also interrogated by DFT calculations over pristine and defect Cu₂(L) (Supplementary Fig. 28) confirming that the defect material will protonate more readily.

Conclusion. In summary, we have electrochemically prepared the Cu₂(L)-e/Cu electrode through controllable growth of MOF nanoparticles onto a Cu-foam support. This integrated electrode composed of a thin compact coating of Cu₂(L) on Cu-foam incorporates uncoupled Cu(II) active sites and shows high conductivity and stability. This electrode shows excellent activity for the electro-reduction of CO₂ to formic acid, with a low onset potential of -1.45 V vs. Ag/Ag⁺, and the FE_{HCOOH} reaches 90.5% at -1.80 V vs. Ag/Ag⁺ with a current density of 65.8 mA·cm⁻². Experimental (EPR spectroscopy) and theoretical (DFT) methods

confirm that the reaction is driven by defects within the structure of the decorated electrode. In Cu₂(L)-e/Cu these defects favour reduction of CO₂ to formic acid versus H₂ evolution. The facile preparation of Cu-MOF-e/Cu electrodes offers an instructive pathway for the development of other efficient materials that catalyse CO₂ reduction at less energetic potentials.

Methods

Materials. Ionic liquids (ILs), EmimOAc (>99%) and EmimBF₄ (>99%) were purchased from Lanzhou Yulu Fine Chemical Co., Ltd. Other chemicals were obtained from Sigma-Aldrich Co., UK.

Ligand synthesis. The ligand H₄L was prepared by the published procedure³⁰. 4-Methylacetophenone (13.4 g, 0.1 mol), terephthalaldehyde (2.70 g, 0.02 mol) and NaOH powder (5.10 g, 0.128 mol) were combined and ground in a ball mill for 90 mins. The resultant solid was dissolved in EtOH (600 mL) with NH₄OAc (30 g, 0.39 mol), and the solution heated under reflux for 24 h. On cooling the white solid was collected by filtration and recrystallised from toluene to yield white crystals. This product (3.0 g) was combined with an aqueous solution of HNO₃ (2 M, 36 mL) and heated in an autoclave to 180 °C for 24 h. The reaction mixture was cooled to room temperature and the solid H₄L was collected and washed with distilled water until the filtrate was pH neutral. The solid was washed further with acetone and dried *in vacuo*.

Characterisations. The morphology of the materials was characterised on a SEM Quanta 650. PXRD analysis was performed on Rigaku Model D/MAX2500 diffractometer using Cu-Kα radiation at a scan speed of 2°/min. Infrared spectra were collected on an iD5 ATR (Attenuated Total Reflection) instrument, and TGA was measured under N₂ at a flow rate of 10 mL·min⁻¹. EPR spectra at X-band and Q-band were recorded using Bruker Micro spectrometers, and the intensity of the EPR signal of different samples was normalised to the sample quantity. The BET surface areas were obtained from N₂ adsorption/desorption isotherms recorded on a Micromeritics 3-Flex instrument at 77 K. CO₂ adsorption isotherms were obtained using Micromeritics 3-Flex at 273 K, 283 K and 298 K, and the value for Q_{st} for CO₂ adsorption was estimated by fitting these isotherms to the Van t' Hoff equation. X-ray photoelectron spectroscopy (XPS) was performed on a Kratos Axis Ultra DLD spectrometer with a monochromated Al-Kα X-ray source (E = 1486.6 eV, 10 mA emission). Fluorescence micrographs were recorded on an Olympus Fluoview FV-1000 instrument to measure the fluorescence generated by the oligomerisation of 1 mL furfuryl alcohol catalysed by 10 mg of MOF at 60 °C over 2 h.

Solvothermal synthesis of Cu₂(L)-t. The solvothermal synthesis of Cu₂(L)-t was conducted by following the literature method³¹. Cu(NO₃)₂·3H₂O (24.2 mg, 0.10 mmol) and H₄L (35.6 mg, 0.05 mmol) were dissolved in DMF (3 mL) with 8 M HNO₃ (0.3 mL). The solution was heated at 80 °C for 48 h in a pressure tube. On cooling to room temperature, the precipitate was collected by centrifugation, washed five times with acetone (10 mL) and dried *in vacuo*.

Electro-preparation of Cu₂(L)-e/Cu. This was performed in a 50 mL single cell using a two-electrode system comprising Cu foam sheets (0.5 cm × 1.0 cm²) as both cathode and anode with a solution of DMF/dioxane/H₂O (2:1:1 v/v/v; 50 mL with 5 drops of aqueous HCl (37%) containing EmimOAc (1.0 mL) as supporting electrolyte. H₄L (33 mg, 0.05 mmol) was dissolved in the electrolyte solution under stirring to form a homogeneous solution. The electrolysis was undertaken for 10 min at 8.0 V and 60 °C. The as-synthesised MOF-decorated electrode was immersed in a mixture of acetone/acetonitrile (1:1 v/v) and the solvent exchanged five times to remove any residual electrolyte and unreacted materials. The preparation of HKUST-1-e/Cu electrode was undertaken using the same method as used for Cu₂(L)-e/Cu but using a different ligand (trimesic acid).

Preparation of electrodes. The Cu₂(L)-e/Cu and HKUST-1-e/Cu were used directly as electrodes. For the Cu₂(L)-t/CP electrode, 5.0 mg of Cu₂(L)-t were suspended in 0.5 mL of isopropanol containing 25 μL of Nafion D-521 dispersion (5 wt%) and treated with ultrasound to form a homogeneous ink. 150 μL of the ink was spread onto the hydrophobic CP (0.5 × 0.5 cm²) surface and dried at 60 °C.

Electrochemical reduction of CO₂. The electro-reduction of CO₂ was carried out on an electrochemical workstation (CHI 660E, USA). LSV and electrolysis were conducted in an H-type cell with a three-electrodes configuration consisted of working electrode, CP (0.5 × 0.5 cm²) as counter electrode, and Ag/Ag⁺ (0.01 M AgNO₃ in 0.1 M TBAP-MeCN) as reference electrode¹². The catholyte and anolyte were 0.5 M EmimBF₄/MeCN and 0.1 M H₂SO₄ aqueous solution, respectively, separated by a Nafion-115 membrane. N₂ and CO₂ were bubbled into the catholyte prior to the experiments. For cyclic voltammetric measurements, a scan speed of 20 mV·s⁻¹ was used over a potential range from -1.2 V to -2.4 V vs. Ag/Ag⁺.

Electrolysis experiments were performed with an initial CO₂ flow rate of 20 mL min⁻¹ prior to the experiment, which was decreased to 10 mL min⁻¹ after the electrolyte was saturated with CO₂. After electrolysis, the gaseous products were collected using a gas bag and analysed by GC and liquid products measured by ¹H-NMR spectroscopy. The Faradaic efficiencies (FE) were calculated using the Eq. (1):

$$FE(\%) = \frac{n_{\text{product}} \times n_{\text{electrons}} \times F}{Q} \times 100\% \quad (1)$$

where n_{product} is the amount of product (mol) from GC (H₂) or ¹H NMR spectroscopy (formic acid), $n_{\text{electrons}}$ is electron transfer number (both the production of H₂ and HCOOH are two-electron processes), F is the Faraday constant (96485 C mol⁻¹), and Q is the total charge passed during the electrolysis of CO₂. The current density for a given product is calculated by multiplying the total current density with FE of the product. The C_{dl} was determined by measuring CV curves at different scan rates. The potential range for the CV tests was from -0.55 V to -0.50 V vs. Ag/Ag⁺. The EIS spectra were recorded at open circuit potential with an amplitude of 5.0 mV (10⁻² to 10⁵ Hz), and the value for R_{ct} obtained by fitting the EIS spectra using the Zview software (Version 3.1, Scribner Associates, USA)^{12,38}.

EPR analysis. EPR spectra were recorded at room temperature, in continuous-wave mode, on Bruker EMX spectrometers (X-band, ca. 9.85 GHz; Q-band, ca. 34 GHz), at mw power of ~0.63 mW and modulation amplitude 10 G; spectra reported herein were typically obtained over an average of 20 scans, and a Bruker strong pitch ($g = 2.0028$) reference was used as a calibrator. Theoretical modelling of the spectra was performed with the EasySpin toolbox within Matlab⁴⁹. The intensity of the EPR signal of different samples was normalised to the quantity of sample.

Calculations of the spectra with EasySpin³⁶ using the iterative spin Hamiltonian in the Eq. (2)^{34,50}:

$$\hat{H} = g\beta\hat{B}\hat{S} + D[\hat{S}_z^2 - 2/3] + E(\hat{S}_x^2 + \hat{S}_y^2) \quad (2)$$

where D and E are the axial and rhombic zero-field splitting parameters, respectively, to give $g_{xx} = g_{yy} = 2.06-2.07$, $g_{zz} = 2.31-2.36$, $D = 0.33-0.35$ cm⁻¹ and $E = 0$ (Fig. 2g and Supplementary Figs. 5 and 6 and Supplementary Table 2). These parameters are in excellent agreement with data for binuclear copper acetate³⁵ and other Cu(II) systems with a [Cu₂(OOCR)₄] paddle wheel structure^{36,51}.

The relative content of monomer [uncoupled Cu(II) centre as defect] and binuclear [within [Cu₂(OOCR)₄] paddlewheels] centres was calculated from the second integrals from simulated EPR Q-band spectra. At Q-band, the entire $S = 1$ spectrum of the binuclear unit is observed hence defining its relative weighting better than that at X-band where the zero-field splitting is comparable to the microwave frequency. The ratio of monomer to binuclear species is obtained from the weighting of the two spin systems (Supplementary Fig. 7; this is illustrated by the second integrals of the simulated components in Supplementary Fig. 8)³⁶. The final monomer to binuclear ratio was obtained by weighting the EPR data by the Boltzmann population of the $S = 1$ state of the binuclear species based upon the Bleaney-Bower equation [(Eq. (3))^{35,36}

$$\frac{nT}{nT + nS} = \frac{3\exp\left(\frac{-\Delta E_{ST}}{RT}\right)}{1 + 3\exp\left(\frac{-\Delta E_{ST}}{RT}\right)} \quad (3)$$

where ΔE_{ST} is the singlet (S)-triplet (T) energy gap (ca. 300 cm⁻¹), nT and nS are the populations at temperature of T , and R is the gas constant.

The relative content of free, uncoupled Cu(II) centres as a function of electrolysis time was measured from the second integral of the signal for this species using X-band EPR spectroscopy. EPR spectra of electrodes were collected every 15 min during electrolysis at -1.8 V vs. Ag/Ag⁺. The obtained EPR spectra were transformed to a second integral value, and all data normalised to the surface area of the electrodes.

DFT calculations. Calculations were based on spin-polarised DFT using projector augmented wave (PAW) methods, as implemented in the Vienna *ab initio* simulation package (VASP)⁵². A plane-wave basis set with a kinetic-energy cut-off of 400 eV was used to expand the wave function of valence electrons. The generalised gradient approximation (GGA) with the Perdew-Burke-Ernzerhof (PBE) functional was used for describing the exchange-correlation interactions⁵³. Vacuum space of 20 Å was set to prevent the interaction between two molecules. The Brillouin-zone integration was sampled by single Γ point. The structural relaxations were performed by computing the Hellmann-Feynman forces within the total energy and force convergences of 10⁻⁴ eV and 0.01 eV/Å, respectively. Based on computational hydrogen electrode (CHE) model⁵⁴, and the Gibbs free energy of an adsorbed intermediate from reduced CO₂ was calculated using $\Delta G = \Delta E + \Delta E_{ZPE} - T\Delta S_{\text{ads}}$, where ΔE , ΔE_{ZPE} and $T\Delta S_{\text{ads}}$ are the electronic adsorption energy, zero point energy and entropy corrections, respectively. The corrections of zero point energy and entropy of different species are shown in Supplementary Table 4. VaspSol, the Poisson-Boltzmann implicit solvation model, was used to describe the effect of solvation⁵⁵, and DFT calculations were implemented via VASP with a

dielectric constant of $\epsilon = 37.5$. The solvation energy was directly contained in the total energy.

Data availability

All relevant data are available from the authors, and/or are included with the manuscript. All other data supporting the findings of this study are available within the Article and its Supplementary Information, or from the corresponding author upon reasonable request.

Received: 11 May 2020; Accepted: 22 September 2020;

Published online: 29 October 2020

References

1. Appell, A. M. et al. Frontiers, opportunities, and challenges in biochemical and chemical catalysis of CO₂ fixation. *Chem. Rev.* **113**, 6621–6658 (2013).
2. Aresta, M., Dibenedetto, A. & Angelini, A. Catalysis for the valorization of exhaust carbon: from CO₂ to chemicals, materials, and fuels. Technological use of CO₂. *Chem. Rev.* **114**, 1709–1742 (2014).
3. Dalle, K. E. et al. Electro- and solar-driven fuel synthesis with first row transition metal complexes. *Chem. Rev.* **119**, 2752–2875 (2019).
4. Liu, J., Thallapally, P. K., McGrail, B. P., Brown, D. R. & Liu, J. Progress in adsorption-based CO₂ capture by metal-organic frameworks. *Chem. Soc. Rev.* **41**, 2308–2322 (2012).
5. Wickramaratne, N. P. et al. Nitrogen enriched porous carbon spheres: attractive materials for supercapacitor electrodes and CO₂ adsorption. *Chem. Mater.* **26**, 2820–2828 (2014).
6. Sun, X. F. et al. MoP nanoparticles supported on indium-doped porous carbon: outstanding catalysts for highly efficient CO₂ electroreduction. *Angew. Chem. Int. Ed.* **57**, 2427–2431 (2018).
7. He, M. Y., Sun, Y. H. & Han, B. X. Green carbon science: scientific basis for integrating carbon resource processing, utilization, and recycling. *Angew. Chem. Int. Ed.* **52**, 9620–9633 (2013).
8. Nam, D. H. et al. Molecular enhancement of heterogeneous CO₂ reduction. *Nat. Mater.* **19**, 266–276 (2020).
9. Andrei, V., Reuillard, B. & Reisner, E. Bias-free solar syngas production by integrating a molecular cobalt catalyst with perovskite-BiVO₄ tandems. *Nat. Mater.* **19**, 189–194 (2020).
10. Dinh, C. T. et al. CO₂ electroreduction to ethylene via hydroxide-mediated copper catalysis at an abrupt interface. *Science* **360**, 783–787 (2018).
11. Wang, Y. R. et al. Oriented electron transmission in polyoxometalate-metalloporphyrin organic framework for highly selective electroreduction of CO₂. *Nat. Commun.* **9**, 4446 (2018).
12. Kang, X. C. et al. Highly efficient electrochemical reduction of CO₂ to CH₄ in an ionic liquid using a metal-organic framework cathode. *Chem. Sci.* **7**, 266–273 (2016).
13. Deng, W. Y. et al. Crucial role of surface hydroxyls on the activity and stability in electrochemical CO₂ reduction. *J. Am. Chem. Soc.* **141**, 2911–2915 (2019).
14. Wakerley, D. et al. Bio-inspired hydrophobicity promotes CO₂ reduction on a Cu surface. *Nat. Mater.* **18**, 1222–1227 (2019).
15. Zhu, Q. G. et al. Carbon dioxide electroreduction to C₂ products over copper-cuprous oxide derived from electrosynthesized copper complex. *Nat. Commun.* **10**, 3851 (2019).
16. Dutta, A., Rahaman, M., Luedi, N. C., Mohos, M. & Broekmann, P. Morphology matters: tuning the product distribution of CO₂ electroreduction on oxide-derived Cu foam catalysts. *ACS Catal.* **6**, 3804–3814 (2016).
17. Wu, J. X. et al. Cathodized copper porphyrin metal-organic framework nanosheets for selective formate and acetate production from CO₂ electroreduction. *Chem. Sci.* **10**, 2199–2205 (2019).
18. Nam, D. H. et al. Metal-organic frameworks mediate Cu coordination for selective CO₂ electroreduction. *J. Am. Chem. Soc.* **140**, 11378–11386 (2018).
19. Bulushev, D. A. & Ross, J. R. H. Towards sustainable production of formic acid from biomass for getting hydrogen and fuels. *ChemSusChem* **11**, 821–836 (2018).
20. Sun, Z. Y., Ma, T., Tao, H. C., Fan, Q. & Han, B. X. Fundamentals and challenges of electrochemical CO₂ reduction using two-dimensional materials. *Chem* **3**, 560–587 (2017).
21. Nitopi, S. et al. Progress and perspectives of electrochemical CO₂ reduction on copper in aqueous electrolyte. *Chem. Rev.* **119**, 7610–7672 (2019).
22. Li, C. W., Ciston, J. & Kanan, M. W. Electroreduction of carbon monoxide to liquid fuel on oxide-derived nanocrystalline copper. *Nature* **508**, 504–507 (2014).
23. Li, C. W. & Kanan, M. W. CO₂ reduction at low overpotential on Cu electrodes resulting from the reduction of thick Cu₂O films. *J. Am. Chem. Soc.* **134**, 7231–7234 (2012).
24. Huang, Y. B., Liang, J., Wang, X. S. & Cao, R. Multifunctional metal-organic framework catalysts: synergistic catalysis and tandem reactions. *Chem. Soc. Rev.* **46**, 126–157 (2017).
25. Han, X., Yang, S. & Schröder, M. Porous metal-organic frameworks as emerging sorbents for clean air. *Nat. Rev. Chem.* **3**, 108–118 (2019).
26. Eason, T. L., Moreau, F., Yan, Y., Yang, S. & Schröder, M. Structural and dynamic studies of substrate binding in porous metal-organic framework materials. *Chem. Soc. Rev.* **46**, 239–274 (2017).
27. Li, L. J. et al. Metal-organic frameworks: a promising platform for constructing non-noble electrocatalysts for the oxygen-reduction reaction. *J. Mater. Chem. A* **7**, 1964–1988 (2019).
28. Liu, T. et al. CoP-doped MOF-based electrocatalyst for pH-universal hydrogen evolution reaction. *Angew. Chem. Int. Ed.* **58**, 4679–4684 (2019).
29. Zhao, S. L. et al. Ultrathin metal-organic framework nanosheets for electrocatalytic oxygen evolution. *Nat. Energy* **1**, 1–10 (2016).
30. Carter, J. H. et al. Exceptional adsorption and binding of sulfur dioxide in a robust zirconium-based metal-organic framework. *J. Am. Chem. Soc.* **140**, 15564–15567 (2018).
31. Verma, G. et al. Partially interpenetrated NbO topology metal-organic framework exhibiting selective gas adsorption. *Cryst. Growth Des.* **17**, 2711–2717 (2017).
32. Ameloot, R. et al. Patterned growth of metal-organic framework coatings by electrochemical synthesis. *Chem. Mater.* **21**, 2580–2582 (2009).
33. Kang, X. C. et al. Integration of mesopores and crystal defects in metal-organic frameworks via templated electrosynthesis. *Nat. Commun.* **10**, 4466 (2019).
34. Mkami H., E. L. et al. EPR and magnetic studies of a novel copper metal organic framework (STAM-I). *Chem. Phys. Lett.* **544**, 17–21 (2012).
35. Karunakaran, C. & Balamurugan, M. *Spin Resonance Spectroscopy*. 169–197 (Elsevier Inc., 2018).
36. Bleaney, B. & Bowers, K. D. Anomalous paramagnetism of copper acetate. *Proc. R. Soc. Lond. A* **214**, 451–465 (1952).
37. Albo, J. et al. Copper-based metal-organic porous materials for CO₂ electrocatalytic reduction to alcohols. *ChemSusChem* **10**, 1100–1109 (2017).
38. Zhu, Q. G. et al. Efficient Reduction of CO₂ into formic acid on a lead or tin electrode using an ionic liquid catholyte mixture. *Angew. Chem. Int. Ed.* **55**, 9012–9016 (2016).
39. Wu, H. R. et al. Design of naturally derived lead phytate as an electrocatalyst for highly efficient CO₂ reduction to formic acid. *Green. Chem.* **20**, 4602–4606 (2018).
40. Lu, L. et al. Selective electroreduction of carbon dioxide to formic acid on electrodeposited SnO₂@N-doped porous carbon catalysts. *Sci. China Chem.* **61**, 228–235 (2018).
41. Jee, B. et al. Continuous wave and pulsed electron spin resonance spectroscopy of paramagnetic framework cupric ions in the Zn(II) doped porous coordination polymer Cu_{3-x}Zn_x(btc)₂. *J. Phys. Chem. C* **114**, 16630–16639 (2010).
42. Song, D. et al. Coordinative reduction of metal nodes enhances the hydrolytic stability of a paddlewheel metal-organic framework. *J. Am. Chem. Soc.* **141**, 7853–7864 (2019).
43. Gao, S. et al. Partially oxidized atomic cobalt layers for carbon dioxide electroreduction to liquid fuel. *Nature* **529**, 68–71 (2016).
44. Wang, X. L. et al. Exploring the performance improvement of the oxygen evolution reaction in a stable bimetal-organic framework system. *Angew. Chem. Int. Ed.* **57**, 9660–9664 (2018).
45. Zhang, L., Zhao, Z. J. & Gong, J. L. Nanostructured materials for heterogeneous electrocatalytic CO₂ reduction and their related reaction mechanisms. *Angew. Chem. Int. Ed.* **56**, 11326–11353 (2017).
46. Feaster, J. T. et al. Understanding selectivity for the electrochemical reduction of carbon dioxide to formic acid and carbon monoxide on metal electrodes. *ACS Catal.* **7**, 4822–4827 (2017).
47. Kortlever, R., Shen, J., Schouten, K. J. P., Calle-Vallejo, F. & Koper, M. T. M. Catalysts and reaction pathways for the electrochemical reduction of carbon dioxide. *J. Phys. Chem. Lett.* **6**, 4073–4082 (2015).
48. Dong, H. L., Li, Y. Y. & Jiang, D. E. First-principles insight into electrocatalytic reduction of CO₂ to CH₄ on a copper nanoparticle. *J. Phys. Chem. C* **122**, 11392–11398 (2018).
49. Stoll, S. & Britt, R. D. General and efficient simulation of pulse EPR spectra. *Phys. Chem. Chem. Phys.* **11**, 6614–6625 (2009).
50. Malik, M. A. et al. The synthesis, spectroscopy and X-ray single crystal structure of catena-[(μ-anacardato)-copper(II)bispyridine][Cu₂{(μ-O₂CC₆H₃(o-OH)(o-C₁₅H₃₁)}₄(NC₅H₅)₂]. *Dalton Trans.* **42**, 14438–14444 (2013).
51. Güdel, H., Stebler, A. & Furrer, A. Direct observation of singlet-triplet separation in dimeric copper(II) acetate by Neutron Inelastic Scattering spectroscopy. *Inorg. Chem.* **18**, 1021–1023 (1979).
52. Kresse, G. & Joubert, D. From ultrasoft pseudopotentials to the projector augmented-wave method. *Phys. Rev. B* **59**, 1758–1775 (1999).
53. Perdew, J. P., Burke, K. & Ernzerhof, M. Generalized gradient approximation made simple. *Phys. Rev. Lett.* **77**, 3865–3868 (1996).

54. Nørskov, J. K. et al. Origin of the overpotential for oxygen reduction at a fuel-cell cathode. *J. Phys. Chem. B* **108**, 17886–17892 (2004).
55. Mathew, K., Sundararaman, R., Letchworth-weaver, K., Arias, T. A. & Hennig, R. G. Implicit solvation model for density-functional study of nanocrystal surfaces and reaction pathways. *J. Chem. Phys.* **140**, 084106 (2014).

Acknowledgements

We thank EPSRC (EP/I011870), the Royal Society (IC170327), National Natural Science Foundation of China (21733011, 21890761), University of Manchester and Institute of Chemistry, Chinese Academy of Sciences for funding, and EPSRC for funding of the EPSRC National EPR Facility at Manchester. This project has received funding from the European Research Council (ERC) under the European Union's Horizon 2020 research and innovation programme (grant agreement No 742401, *NANOCHEM*). J.L. thanks China Scholarship Council for funding. X.K. and A.S. are supported by Royal Society Newton International Fellowships. We thank Dr. M. Shanmugam, Mr. A. Brookfield and Dr. S. Lockyer for their kind support with some of the EPR measurements.

Author contributions

X.K., L.Li, X.H., J.L. and L.Liu: syntheses and characterisations of MOF samples and catalysis studies. L.Li, A.S., F.T. and E.J.L.M.: collection and analysis of EPR data. X.K. and B.H.: DFT calculation. B.H., S.Y. and M.S.: overall design and direction of the project. X.K., B.H., S.Y. and M.S.: preparation of the manuscript with help from all authors.

Competing interests

The authors declare no competing interests.

Additional information

Supplementary information is available for this paper at <https://doi.org/10.1038/s41467-020-19236-4>.

Correspondence and requests for materials should be addressed to B.H.; , S.Y.; or M. Söd.

Peer review information: *Nature Communications* thanks Zhi-Yuan Gu, Hervé Vezin and the other, anonymous, reviewer(s) for their contribution to the peer review of this work. Peer reviewer reports are available.

Reprints and permission information is available at <http://www.nature.com/reprints>

Publisher's note Springer Nature remains neutral with regard to jurisdictional claims in published maps and institutional affiliations.



Open Access This article is licensed under a Creative Commons Attribution 4.0 International License, which permits use, sharing, adaptation, distribution and reproduction in any medium or format, as long as you give appropriate credit to the original author(s) and the source, provide a link to the Creative Commons license, and indicate if changes were made. The images or other third party material in this article are included in the article's Creative Commons license, unless indicated otherwise in a credit line to the material. If material is not included in the article's Creative Commons license and your intended use is not permitted by statutory regulation or exceeds the permitted use, you will need to obtain permission directly from the copyright holder. To view a copy of this license, visit <http://creativecommons.org/licenses/by/4.0/>.

© The Author(s) 2020